Modal behavior observed in the evolution of immiscible interfaces within an injection-forced Hele-Shaw cell

Jerry Wiggert
Ocean Physics Group, Department of Geological Sciences, University of Southern California, Los Angeles, California 90089-0740

Tony Maxworthy
Departments of Mechanical and Aerospace Engineering, University of Southern California, Los Angeles, California 90089-1191
(Received 31 August 1992; revised manuscript received 13 January 1993)

A series of experiments has been performed on a horizontally oriented, rectangular Hele-Shaw cell. Air was injected in the middle of one of the short sides of the cell into the silicon oil contained between the glass plates of the cell. The resulting unstable, immiscible interface resulted in a series of fingering patterns that were photographed and digitized. A variety of analytical techniques was applied to the images in order to quantify the observed phenomena. These included (i) calculating pattern densities, as a function of distance from the injection port, which help to identify growth regions, (ii) determining power-law relations between several of the patterns' growth parameters (e.g., interface length, gyration radius, and flow area), and (iii) obtaining time series of two fractal measures, thus illustrating temporal variability in the geometrical properties of the images. In addition, an extensive study of the distributions of length scales and their temporal evolution was done using histograms with two bin regimes and scatter plots of percent population within given bins. The temporal evolution of dominant scales and a modal distribution of length scales conforming to the predictions of linear stability has been witnessed.

PACS number(s): 68.70.+w

INTRODUCTION

In this series of experiments, a rectangular Hele-Shaw cell was used to study the temporal evolution of the two-dimensional (2D), injection-forced, immiscible interface between air (the forcing fluid) and a silicon oil (Dow Corning 200). The oil was dyed for visualization and was found to have a surface tension (T_s) of 21.0±0.4 dyn/cm, a molecular viscosity (μ) of a 1.066 g/cm sec, and a density (ρ) of 0.96 g/cm^3. The viscosity and density of the air were negligible when compared with that of the oil.

Fluid flow within a Hele-Shaw cell is assumed to locally obey a plane Poiseuille velocity-pressure gradient relationship:

$$u=\frac{-b^2}{12\mu}\text{grad}(P) \tag{1}$$

(where b is a gap width and μ is fluid viscosity). Gravitational terms have been disregarded, since the experiments were done using a horizontal cell. Linear stability analysis [1,2] derives the following dispersion relation for a plane interface:

$$\sigma(\mu_1+\mu_2)=k(\mu_1-\mu_2)V-\frac{k^3T_sb^2}{12} \tag{2}$$

(where σ is the growth rate, V is the magnitude of the interfacial velocity, T_s is the surface tension, and k is the wave number). Temporarily disregarding the surface tension term allows one to see that for $\mu_1<\mu_2$ (subscript 2 refers to the intruding fluid), σ is negative and instabilities will be damped out. The opposite case leads to growing instabilities for which the surface tension creates a threshold or cutoff wave number. The wavelength at which this occurs, i.e., at which σ becomes positive, is the minimum scale needed for the instability to grow and is termed the critical wavelength [l_c, Eq. (3)]:

$$l_c=\pi b\left[\frac{T_s}{3V(\mu_1-\mu_2)}\right]^{1/2}. \tag{3}$$

The length scale (l^*) at which the maximum growth rate is attained has been worked out [1] to be $l^*=\sqrt{3}l_c$. This length scale was used to calculate characteristic parameters, described below in Table I, which serve to create dimensionless results.

These solutions were obtained assuming *ad hoc* that the pressure drop across the interface was of the form

$$\Delta P=T_s\left[\frac{2}{b}+\frac{1}{R}\right], \tag{4}$$

where R is the radius of the meniscus projected onto the plates. This assumption has been the subject of much discussion (see [3] for a comprehensive discourse). It ignores corrections in the interfacial pressure condition due to changes in the gap width caused by the residual film of more viscous fluid left on the plates. These wetting effects have been accounted for, to first order, and the 3D free-boundary problem at the fluid interface has been solved, through the use of a double expansion around N_{ca} (the capillary number) and the ratio of the interface's transverse and lateral dimensions [4]. This work resulted in an expression for the pressure drop [Eq. (5)], where $N_{ca}=V\mu_1/T_s$ and $J=3.8$:

$$\Delta P = T_s \left[\left(\frac{2}{b} + \frac{\pi}{4R} \right) + \frac{2J}{b} N_{ca}^{2/3} \right]. \quad (5)$$

The first-order boundary condition and results of numerical experiments for the dynamically similar flow in a tube [5] have been utilized to develop a relation for the modified wave number [6], defined below:

$$A_{max} = k_{max} b N_{ca}^{-1/2}. \quad (6)$$

Curves for the various theoretical predictions and the results of laboratory experiments have been concisely summarized (Fig. 2 of [7]). These curves reveal that for low N_{ca} the formulations developed using Eq. (5) show good correspondence, but as the flow rate is increased, the experimental data for A_{max} is significantly lower than the theoretical predictions. In fact, in the limit of large N_{ca} the most unstable wavelength becomes a constant multiple of the gap width.

When performing experiments with a Hele-Shaw cell, the extruded fluid can be seen to leave a thin film on the plates as it is displaced. This residual film, alluded to in the preceding paragraph, narrows the gap through which the intruding fluid can flow. This causes the pressure change across the interface to rise, resulting in an increased interfacial velocity through mass conservation. Equation (3) indicates that the threshold length scale decreases as the interfacial velocity increases, thus leading to a more convoluted growth pattern. Indeed, it was possible to distinguish regions of higher interfacial velocity by the presence of shorter-wavelength instabilities as well as a residual film of varying thickness, which may be seen in the photographs (Fig. 2) but which proved impossible to quantify.

The air space at the top of the cell, necessary for unrestricted fluid evacuation, led to the presence of an upper air-oil interface. This second interface (Fig. 2) was also digitized in an attempt to create a fluid volume budget which might be used to estimate the average thickness of the residual film. However, this budget could not be accurately determined, since not all of the fluid was driven towards the top of the cell. This was emphasized by the occurrence of a "pinching-off" phenomena which happened more frequently as the flow rate was increased [Fig. 2(c)]. This was due to the displaced oil being pushed to the sides of the cell and returning towards the injection port along the cell boundaries. As this return flow propagated along the sidewalls, it compacted the existing flow pattern. Normally, this was insignificant, i.e., the existing flow pattern was not noticeably affected. The return flow was of importance only when a thin region of the flow pattern near the injection port was pinched shut by the downward propagating oil. This caused the flow pattern to be separated into an actively forced region and one or more freely floating globule(s). This pinching-off phenomena limited the useful range of flow rates for the experiments, resulting in a limited range of length scales.

EXPERIMENTAL PROCEDURE

The cell consisted of two glass plates of thickness 1.27 cm separated by a gap of 0.21 cm and a visible surface of 61 by 120 cm. Instead of generating a gravitationally driven instability by rotation about its central axis [8], the cell was kept horizontal and forcing was accomplished through air injection. In the upper plate five holes were drilled (Fig. 1), into which one thermistor and four valves were fitted. The cell was not completely filled with the viscous oil in order to allow for the presence of the air pocket, which could exit from the top of the cell with minimal resistance when air was injected at the bottom.

The experiments consisted of six runs each at three different flow rates and five runs at the highest flow rate. For each run, between 10 and 13 pictures were taken using a 35-mm camera with an electric winder. An electronic timer was attached to the cell and included in the photographs. Each series of photographed interfaces (Fig. 2) was then projected, using a dark-room enlarger, onto a digitizing pad (GTCO Demi-Pad 5) where they were digitized by hand. The generated data were stored on an IBM-PC. This procedure resulted in a resolution of 8.2 points/cm for the stored images. Once on the computer, various analytic techniques were developed and applied to the images in order to quantitatively describe the interface evolution.

RESULTS AND OBSERVATIONS

Pattern evolution

After starting out as a semicircle near the injection port [Fig. 2(a)], the flow pattern quickly evolves into two major fingers growing towards the top of the cell [Figs. 2(b) and 3(a)]. These two major fingers frequently bifurcate along the tips and sides, at the latter of which the growth is quickly damped by the presence of the side walls. When the fingers split at the tip, a growth competition develops, and it can be seen that the eventual winner has a more convoluted interface, indicating a greater mass flux into that finger. As the faster-growing finger outpaces its competitor, it begins to spread laterally, thus shielding the slower finger from any further expansion towards the top of the cell. These three mechanisms, interface bifurcation, shielding by competing fingers, and flow restriction by cell boundaries, combine in the formation of the observed fingering patterns.

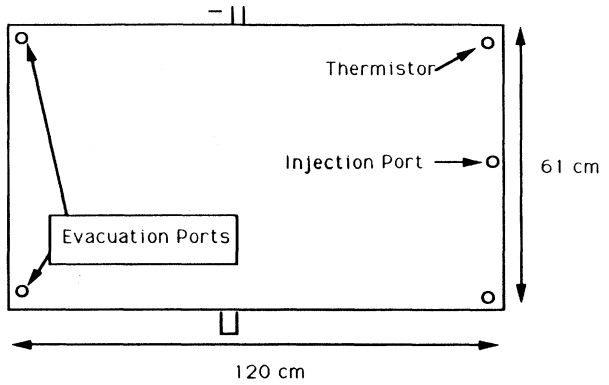

FIG. 1. Schematic of rectangular cell used for experiments.

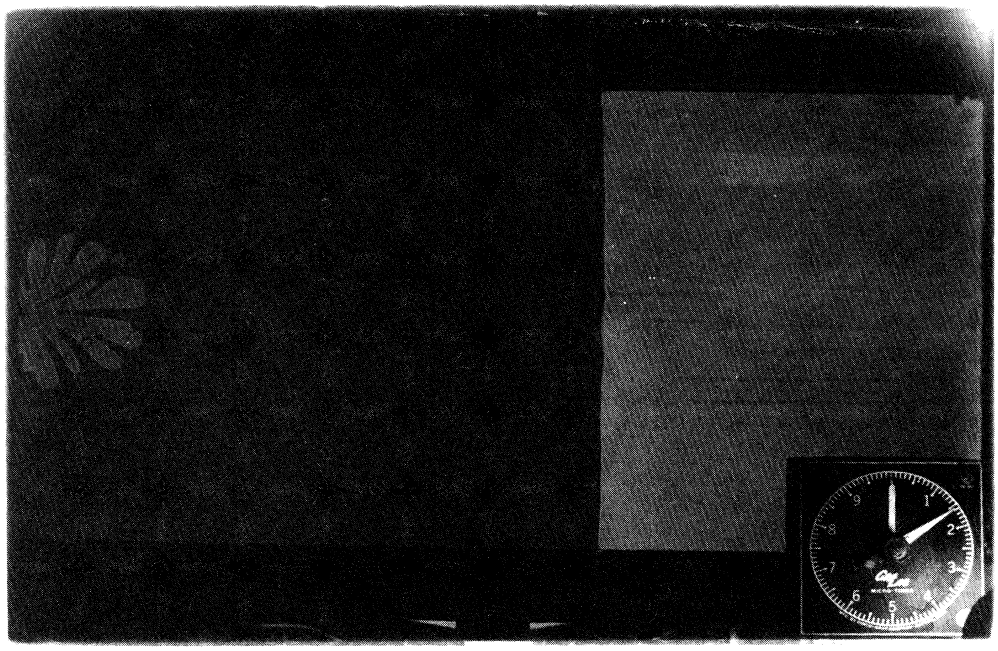

(a)

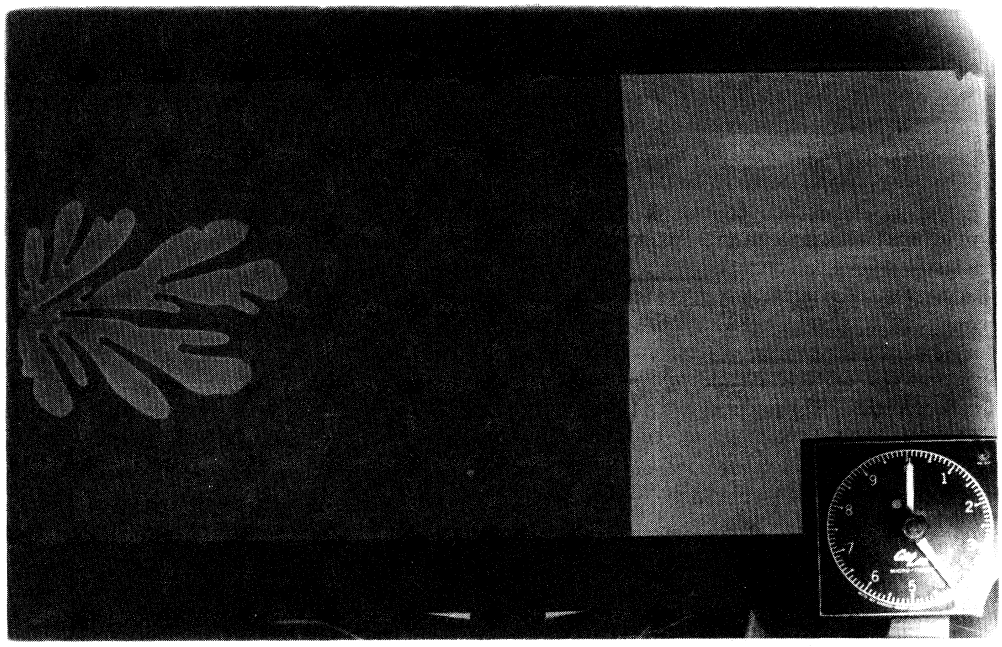

(b)

FIG. 2. (a) Frame 2 of a run from the highest flow rate. This picture illustrates the semicircular nature of the growth away from the injection port, before the presence of the side walls is felt. (b) Frame 5 of the same run. This picture shows the expansion to be essentially parallel to the side walls and the occurrence of a growth competition between two main fingers. (c) Frame 8 of the same run. This picture illustrates the pinching-off effect (the upper left portion of the pattern has become disconnected), which occurred for several of the runs at higher flow rates.

(c)

FIG. 2. (*Continued*).

The bifurcation spacing has been quantized by taking slices through the digitized flow pattern, parallel to the bottom wall, at equally spaced distances above the injection point. The ratio of the length of the slice which intersects the injected air normalized by the cell width has been defined as the pattern density (ρ) and plotted as a function of distance from the injection point. These curves [Figs. 3(a) and 7(a)] show that $\rho(y)$ generally oscillates between values of 15% and 40% of the cell width. Comparison of digitized images with their corresponding pattern density curves [Figs. 3(a) and 7(a)] reveal that the local minima of $\rho(y)$ correspond to both pattern bifurcations and, to a lesser degree, the ceasing of a finger's growth due to shielding. The maxima occur when there are several fingers growing simultaneously at a given level. A comparison of pattern density curves of the last frame of different runs shows that there is little correspondence a few cm from the injection port (not shown), indicating that the experimental apparatus is not "seeding" the bifurcations. Superimposing the $\rho(y)$ curves for all frames of a run [Fig. 3(b)] reveals that the evolution of the flow near the injection port eventually ceases and that the pattern retains its basic shape after growth at a level has stopped.

Characteristic parameters

Geometrical characteristics, consisting of the flow area (A), interface length (L_i), gyration radius [R_g, defined as $(\int_0^{H_F}\rho(y)y\,dy)^{1/2}$] and flow height ($H_f$) were determined for each digitized pattern. The interfacial velocity (V) was estimated by linearly regressing R_g against time, with the minimum correlation coefficient for all runs being 0.996. This is a rough estimation, since it actually measures the motion of the mass centroid, whereas the velocity is nonconstant along the interface. This "integrated" interfacial velocity is used to determine the parameters I^*, u^*, t^*, and B^* defined at the bottom of Table I, similar to those used previously [8] and based upon the linear theory [2]. As a means of comparison with other experiments in the literature, N_{ca} ranges in value from 0.129 to 0.222 for these experiments. The parameter I^* was limited by the pinching-off phenomena to a range of 1.84 cm down to 1.40 cm for the highest flow setting.

Power-law relations (with exponents a, c, d, and e) corresponding to the relationship between the four parameters [L_i, R_g, time (t), and H_f] and the flow area (A) have been calculated and are shown in Table I, together with their definitions. An example of each relation, corresponding to the data from the entire run for the flow pattern in Fig. 3(a), is shown in Fig. 4. The average value for d [1.00 with a standard deviation (hereafter, σ_{SD})$=0.103$] reveals the growth rate of the area to be linear with time, as is to be expected for a constant mass flux. This suggests that the product of H_f and the average width of the pattern w_{av} [defined as $1/H_f\int_0^{H_f}\rho(y)dy$] should vary linearly with the area. In Fig. 4, H_f grows like $A^{0.76}$ (Table I), which indicates that w_{av} should grow like $A^{0.24}$ in order for their product to be linear with the area. This is indeed the case as w_{av} is found to vary like $A^{0.23}$ for this run. Another characteristic of note is the curvature which appears in the scatter plot of H_f versus the area (Fig. 4), indicating that the flow's tip velocity increases with time. This increased velocity is also indicated by the density plots (Fig. 3,7) which show maximum widths to occur near the injection port and a trend toward narrower widths as the flow progresses away from the injection point. Thus, as the patterns spread less la-

terally, they must compensate by growing faster parallel to the walls, hence the increased tip velocity.

The average values for the power relations ($a_{av}=1.30$, $c_{av}=1.27$, and $e_{av}=1.27$, with $\sigma_{SD}=0.044$, 0.049, and 0.051, respectively) are not significantly different. The fact that c_{av} and e_{av} (power relations based on R_g and H_f, respectively) are identical is not surprising, considering that both parameters correspond to one-dimensional growth. Since the interface length should be free to expand in two dimensions, it is difficult to explain why a_{av} is not statistically different from c_{av} and e_{av}. Indeed, for an object with a convoluted 2D interface, the value of a should be less than c and e and should decrease as the interface becomes more convoluted. This is supported by some preliminary experiments performed in a circular cell for which the value of a was 0.5, while c and e were

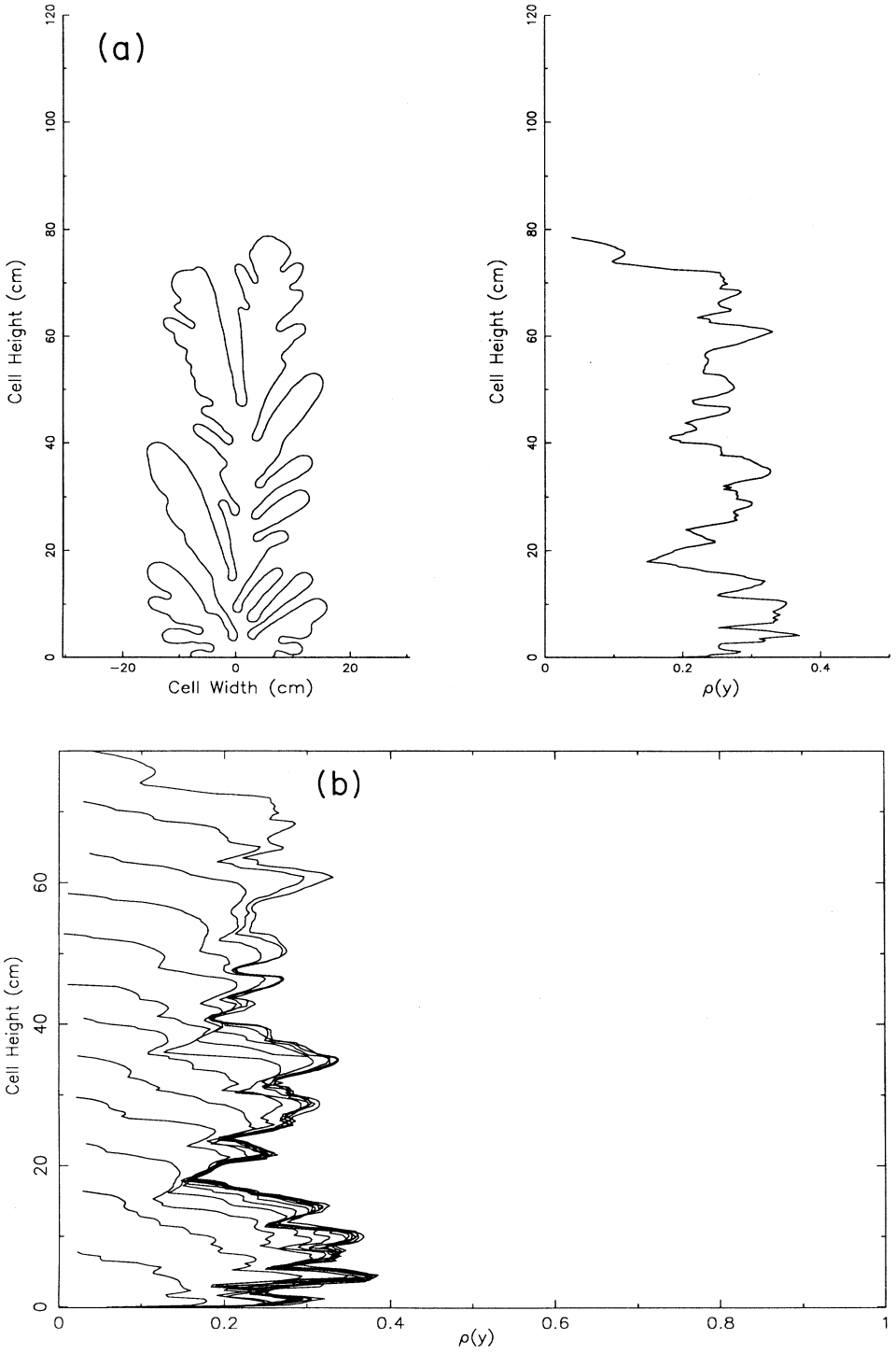

FIG. 3. (a) Digitized flow pattern and corresponding density curve. Minima in $\rho(y)$ correspond to multiple pattern bifurcations, while maxima correspond to the presence of multiple developed fingers. (b) Superimposed density curves revealing regions of the pattern which have stopped growing. The pattern shown in (a) is the last image of the series shown here.

TABLE I. Hele-Shaw data. Symbol definitions: A is the area, L_i is the interface length, R_g is the gyration radius, t is time, H_f is the flow height, $V = DR_g/dt$; exponents defined as: $A = L_i^a$, $A = R_g^c$, $A = t^d$, $A = H_f^e$, b is the plate gap, μ_1 is the viscosity of oil, μ_2 is the viscosity of air, T_s is the surface tension, W is the width of the cell. Dimensionless parameters: $I^* = \pi b[T_S/V(\mu_1 - \mu_2)]^{1/2}$, $u^* = V(\mu_1 - \mu_2)/(\mu_1 + \mu_2)$, $t^* = I^*/u^*$, $B^* = I^*/W$.

Flow no.	V (cm/sec)	a	c	d	e	I^*	u^*	t^*	B^*	Images	Pinch-off	Reattach
26	2.601	1.27	1.27	0.94	1.24	1.816	2.600	0.699	0.0298	11	NA	NA
36	2.534	1.32	1.39	1.05	1.37	1.840	2.533	0.726	0.0302	12	NA	NA
17	3.011	1.27	1.26	0.89	1.26	1.688	3.010	0.561	0.0277	11	< 12.1 sec	NA
27	3.216	1.26	1.23	1.02	1.23	1.633	3.215	0.508	0.0268	13	NA	NA
37	3.064	1.30	1.21	1.01	1.20	1.673	3.063	0.546	0.0274	12	NA	NA
57	3.119	1.27	1.31	1.06	1.32	1.658	3.118	0.532	0.0272	12	NA	NA
67	3.095	1.34	1.31	1.02	1.33	1.665	3.094	0.538	0.0273	13	NA	NA
18	3.377	1.42	1.25	0.71	1.20	1.594	3.376	0.472	0.0261	12	< 9.79 sec	NA
28	3.648	1.35	1.29	1.07	1.26	1.534	3.647	0.421	0.0251	12	< 11.7 sec	NA
38	3.692	1.27	1.26	1.05	1.29	1.524	3.691	0.413	0.0250	13	< 11.3 sec	NA
48	3.767	1.36	1.25	1.06	1.25	1.509	3.766	0.401	0.0247	12	NA	NA
58	3.300	1.28	1.34	0.79	1.34	1.612	3.299	0.489	0.0264	11	NA	NA
68	3.601	1.27	1.18	1.01	1.19	1.544	3.600	0.429	0.0253	11	< 10.8 sec	< 11.7 sec
19	4.366	1.29	1.23	1.07	1.22	1.402	4.365	0.321	0.0230	11	NA	NA
29	4.173	1.26	1.28	1.05	1.26	1.434	4.171	0.344	0.0235	8	NA	NA
39	3.942	1.28	1.31	1.08	1.30	1.475	3.941	0.374	0.0242	10	< 7.7 sec	< 8.7 sec
49	3.932	1.26	1.29	1.06	1.28	1.477	3.930	0.376	0.0242	13	< 6.7 sec	NA
59	4.288	1.28	1.26	1.03	1.26	1.415	4.286	0.330	0.0232	12	< 8.9 sec	< 10.5 sec

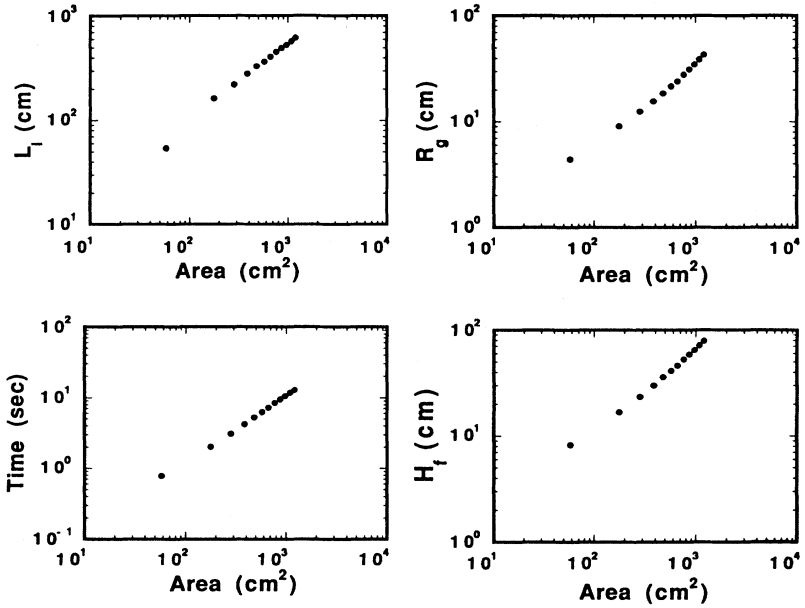

FIG. 4. Examples of the graphs of various flow characteristics plotted vs the flow area and used to determine the power-law parameters for each series of images. These data are from the run shown in Fig. 3.

1.5 and 0.8, respectively. This suggests that the rectangular cell geometry is restricting the growth of the interface such that its increase due to the instability mechanism is insignificant when compared to its increase in the along cell direction.

Pattern parametrization using fractal dimensions

Fractal dimensions have been recently popularized as a means of quantifying the geometry of non-Euclidean objects [10]. Richardson [11] employed the stick method while puzzling over the fact that the total length of a given geographical boundary was sometimes reported in different sources with a variation of up to 20%. He found that geographical boundaries increased in length as the measuring gage was decreased in size. Another way of estimating a fractal dimension is the box-counting method. This technique consists of superimposing a rectangle over the object of interest, subdividing the rectangle, and recording the number of boxes covering a portion of the flow for each subdivision. Ideally, the shape being analyzed will have spatial variability over a range of length scales so that the gage length may be varied over several orders of magnitude in order to have a well-defined dimension. A dimension (D) is determined by setting the nominal Euclidean dimension (1 or 2) equal to the value of the constant slope which appears in a log-log plot of the number of steps or boxes versus gauge length when analyzing a fractal object. In this analysis, two fractal dimensions, defined as the interfacial dimension (D_i, using the stick method) and the area dimension (D_a, using the box-counting method), have been calculated. The curves used for finding the two dimensions for the flow pattern shown in Fig. 3(a) are shown in Figs. 5(a) and 5(b). Both dimensions have been calculated for each image of the experiment, and Figs. 6(a) and 6(b) consist of scatter plots of all the dimension estimates (D_i and D_a, respectively) as a function of time, allowing for investigations of temporal variability.

The range of gage lengths used for the two methods was limited to one order of magnitude by fluid and geometrical properties. The minimum gage length (3 mm) was chosen to be between the digitizing resolution (≈ 1.2 mm) and the smallest value for the critical (i.e., growth threshold) wavelength ($l^*/\sqrt{3} \geq 8.1$ mm, Table I) for all the runs analyzed. The maximum gage length was limited to 3.6 cm by the onset of a "sporadic" result in the interfacial dimension [Fig. 5(a)] which occurred when analyzing the interfaces from the early images of a run. This behavior is due to these short interfaces having total lengths not much greater than the maximum gage length and was also seen in the area dimension curves to a lesser degree [Fig. 5(b)]. The maximum limit could have been increased as the interface length increased, but was kept constant in order to have a consistent technique that allowed for comparison between frames.

In order to obtain a value for D_i from the log-log plots, a least-squares fit was applied to the data points. This was done to reduce biasing, since it was difficult to objectively determine a constant slope region on some curves. The scatter plot of all D_i time series from the experiment and the superimposed third-order-polynomial curve fit [Fig. 6(a)] reveal that the interface dimension starts near 1.20 before reaching an asymptotic value of 1.07. The highest values always correspond to the initial image for which the length scales are severely limited. It is possible that the elevated values of D_i for the initial images of a run are a by-product of the extremely limited range of length scales due to the interface length's limited magnitude. This restriction makes it difficult to determine an interfacial dimension for the initial images of a run, and it may be that the wide variation in D_i over the course of

a run should be viewed with skepticism. D_a is obtained using the same curve-fitting method used to determine D_i. The scatter plot of all the D_a time series from the experiment [Fig. 6(b)] shows that the values of D_a range from 1.77 to 1.82 with a slight increase as the pattern develops, followed by a slight decrease near the end of the run.

When comparing the scatter plots for the two different dimensions [Figs. 6(a) and 6(b)], two characteristics are immediately obvious. The data on the D_i curve reveals greater scatter ($\sigma_{SD}=0.035$) and a stronger time dependence than the D_a data ($\sigma_{SD}=0.011$). This is especially pronounced for the earlier times of a run where the initial values for D_i range from 1.11 to 1.22, while D_a ranges from 1.77 to 1.81. The temporal variability of the two time series is emphasized by the third-order-polynomial curve fits which have been superimposed on the scatter plots. The curve fits are useful in obtaining an averaged behavior for the data from the entire experiment and provide a means of comparing the overall trends of the interfacial and area dimensions. The general characteristics of the curve fits for the two-dimensional measures have already been briefly discussed, and some doubts have been raised concerning the validity of the indication in the D_i plot that the dimension of the patterns decreases with time. However, the curve fit for the D_a data shows some indication of corroborating this possibility. It should be remembered that the area dimension will tend toward 2.0 as the object under investigation becomes less fractal. Keeping this in mind, the curve fit for D_a is at its lowest value at the beginning of the time series when D_i is at its peak. As D_i decreases towards its asymptotic value, D_a increases. Although the variation in D_a is slight, it does vary in such a manner as to support the observed variation in D_i.

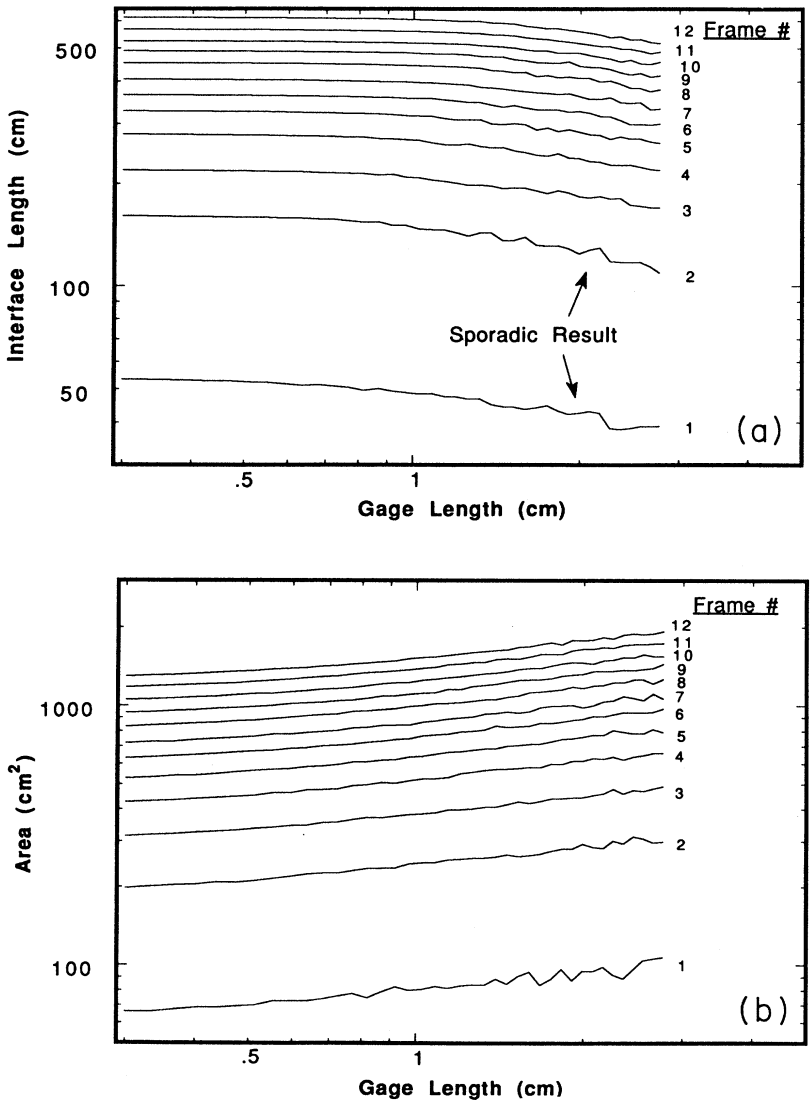

FIG. 5. (a) The complete series of interfacial dimension plots generated for the flow patterns of Fig. 3. (b) The complete series of area dimension plots generated for the flow patterns of Fig. 3.

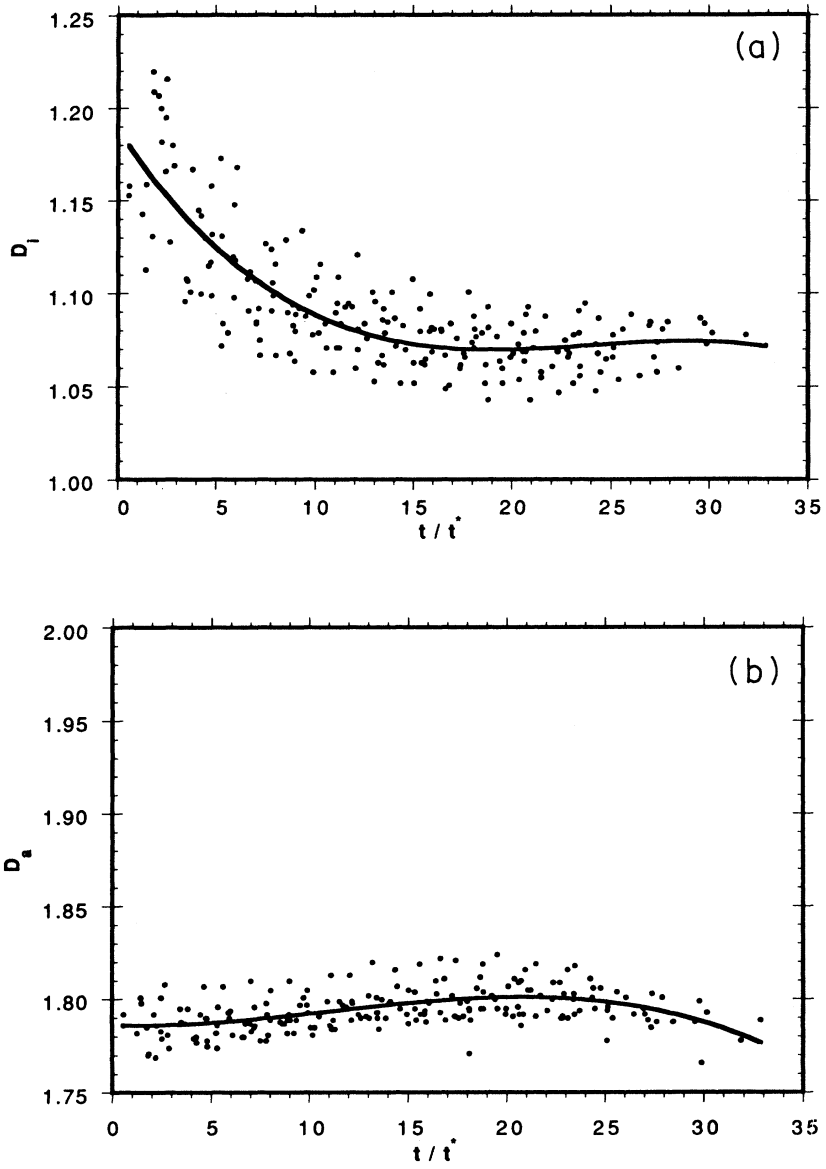

FIG. 6. (a) Interfacial dimension estimates for the entire experiment plotted as a function of dimensionless time. The third-order-polynomial curve fit is shown. (b) Area dimension estimates for the entire experiment plotted as a function of dimensionless time. The third-order-polynomial curve fit is shown.

Spatial scale distribution and temporal variability

The local radius of curvature of the flow pattern has been determined by stepping along the interface and calculating the radius of the circle circumscribing a local triad of interfacial coordinates. These radii have also been inverted to obtain the curvature of the interface. A sign convention has been introduced in which positive values correspond to a curvature directed away from the injection point (i.e., the center of the fitted circle lies outside the injected air) and vice versa. The spatial distribution and temporal variability of the length scales generated by the instability mechanism are illustrated using (1) plots of curvature as a function of interfacial position (starting at the injection port and traversing the interface in a clockwise direction before returning to the injection port), (2) histograms of radius, and (3) time series of population percentage within bins which are defined based on the length scales obtained from the stability analysis.

The curvature plots [Figs. 7(b) and 7(c)] reveal the spacing of the growth regions along the interface and the onset of pinch off events. The position of the small-scale concentrations (i.e., the growth regions) is determined by the state of the fingering competition along the interface. If there is one dominant finger in the expanding region of the flow [Fig. 7(a)], then the concentration of small scales will straddle the halfway point of interfacial position [Fig. 7(b)], corresponding to the top of the pattern. If there are two growing fingers of unequal size (Fig. 4), then two regions of small scales will be concentrated around a region of larger scales [Fig. 7(c)] and will not necessarily be symmetric about the halfway point. In ad-

dition, in the growth regions containing the smallest scales, the negative scales outnumber the positive scales.

The limit definitions for the nine bins in the time series of percent population are defined in Table II, along with the average value for the population, the standard deviation,and a brief description of the temporal behavior. The different bins can be divided into three categories. A representative for each category is shown in Figs. 8(a)–8(c). The percent population in bins 1 and 9 tends to increase with time [Fig. 8(a)], although the trend is difficult to discern. The greatest rate of increase comes for $t/t^* \leq 5.0$. Bins 2, 6, 7, and 8 show their percent populations to be relatively constant [Fig. 8(b)]. Bin 2 shows a slight decreasing trend but the scatter is too high

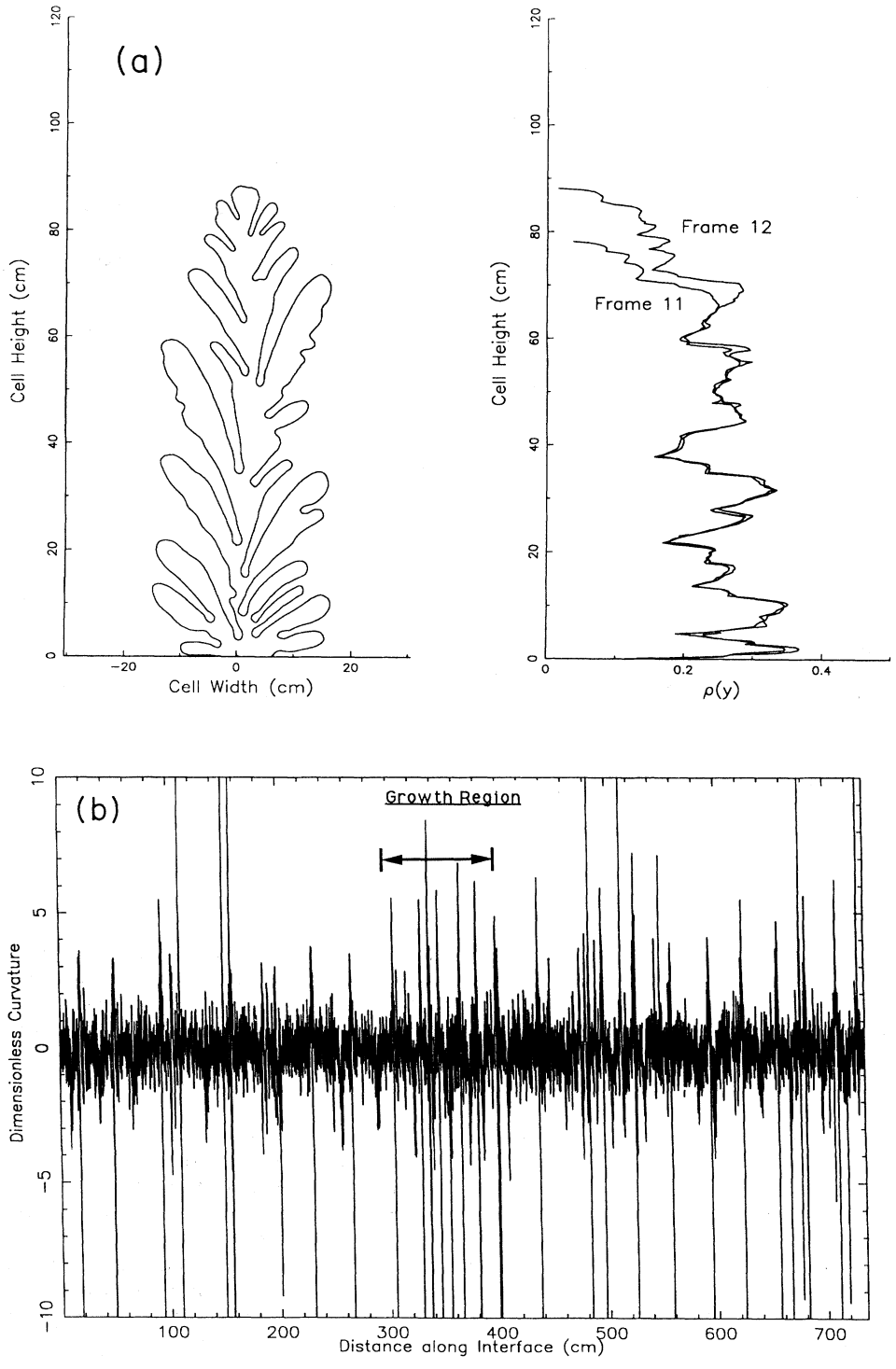

FIG. 7. (a) Flow pattern and density curve corresponding to curvature plot in (b). The second density curve is the previous frame of the run. The growth region is indicated by the numerous bifurcations and the divergence in the two density curves above 65 cm. (b) Dimensionless curvature as a function of distance along the interface. Note the high concentration of negative length scales around 350 cm corresponding to the new growth region illustrated in (a). (c) Dimensionless curvature as a function of distance along the interface. This plot coresponds to the image shown in Fig. 3(a). Note the multiple concentrations of small length scales centered at 185, 220, and 340 cm along the interface. This is due to there being two competing fingers with separate growth regions instead of one dominant finger with a single growth region.

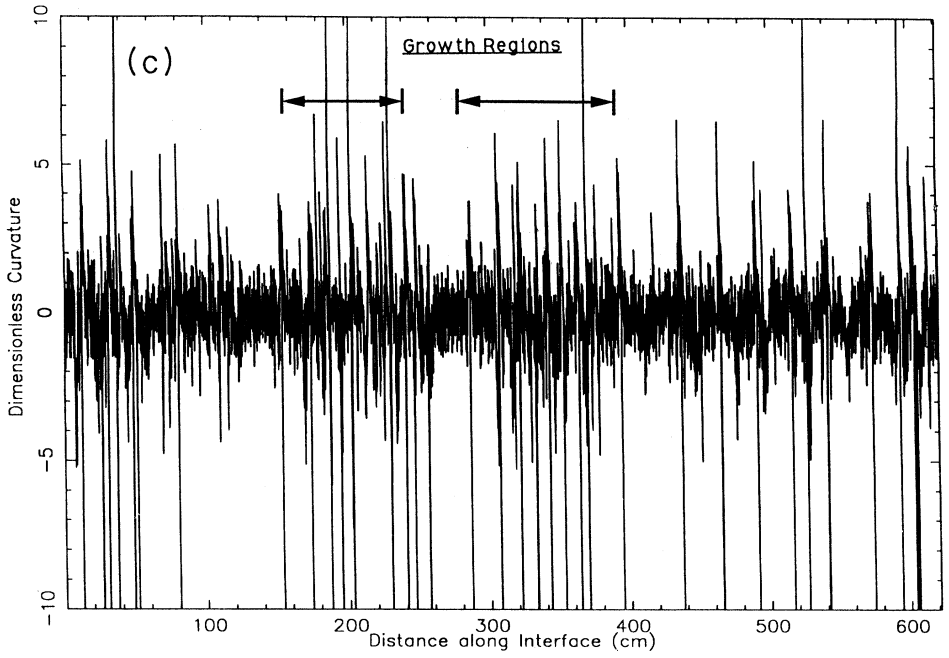

FIG. 7. (*Continued*).

to make a definitive statement. Bins 3, 4, and 5 have percentage populations that decrease with time. All four of these bins show the greatest rates of decrease for $t/t^* \leq 5.0$ [Fig. 8(c)]. The overall picture presented by these time series plots is one of a trend toward spatial scales of increasing magnitude.

Histograms of radii have been formed to study the distribution of scales with respect to the characteristic lengths predicted by the linear theory. The values of the abscissa have been normalized by I_c, so values of ± 1.0 correspond to $\pm I_c$. An average large bin histogram has been created (Fig. 9) with error bars indicating the variability found in each bin. These large bins are centered around integer multiples of I_c and are based on the limits and labeled according to the numerical designations found in Table II. Histograms for each image of a run have also been created (Fig. 10). These superimpose the large bins just described upon histograms for which the bin size is taken as $0.1I_c$. This superposition allows for investigations into the position of the dominant modes within the large bins.

The average histogram (Fig. 9), where each bin is labeled according to the bin numbers defined in Table II, reveals the length scale distribution over the entire experiment. In general, it can be seen that the populations of the negative scales are higher than that of the positive scales for corresponding bins and that the smaller scales have higher populations than the larger scales (within the limits of the histogram) except for bin 5. This is to be expected since the range of attainable length scales has a lower limit of $\pm 0.25I_c$. Bin 4 (delineated by $-1.5I_c$ and $-0.5I_c$) has the highest average probability density function (PDF) and the greatest variability, the latter of which is a result of the ephemeral presence of length scales near $-0.5I_c$. Bin 3, which contains the $-2I_c$ mode, has the second highest average PDF. Bins 6 and 7, the positive counterparts to bins 4 and 3, have the next two highest average PDF's and preserve the trend shown in the negative bins with respect to dominance of shorter scales over longer scales. Indeed, the relative dominance

TABLE II. Large bin limits and characteristics.

Bin no.	Limits	Av. % Pop.	σ_{SD}	Description
1	$< -3.5I_c$	17.9	1.9	increasing, scattered
2	$-3.5I_c - -2.5I_c$	7.9	1.9	constant, slight decrease
3	$-2.5I_c - -1.5I_c$	12.4	1.5	decreasing, scattered
4	$-1.5I_c - -0.5I_c$	14.9	3.0	decreasing, scattered
5	$-0.5I_c - 0.5I_c$	5.3	2.6	decreasing, tight
6	$0.5I_c - 1.5I_c$	10.9	1.4	constant
7	$1.5I_c - 2.5I_c$	9.3	1.6	constant
8	$2.5I_c - 3.5I_c$	6.3	1.4	constant
9	$> 3.5I_c$	19.6	1.6	increasing, scattered

between the two pairs of corresponding postive and negative bins (i.e., bin 4 versus bin 6 and bin 3 versus bin 7) is statistically significant. This is not the case for the final pairing (bins 2 and 8) which have average levels that preserve the domination of negative scales over positive scales. However, the difference in level of these two bins is not statistically significant as illustrated by the error bars on the figure.

The small bin histogram for the lowest flow rate [Fig. 10(a)] reveals the main peaks in scale distribution to be slightly below ± 1.0 with secondary peaks occurring $\approx \pm 1.8$. In addition, the secondary peak at $+1.8$ is rivaled by a peak at $+0.5$. Figures 10(b) and 10(c) are from two different times within the same run of a higher flow rate than that shown in Fig. 10(a). Taken together, they corroborate the tendency toward larger length scales with the progression of time witnessed in Figs. 8(a)–8(c). Figure 10(b) shows the second largest peak in the large bins as ranging from -0.5 to 0.5 and the strongest peak in the small bins to be straddling ± 0.5. The presence of these smaller scales is typical of the earliest pattern evolution images throughout the experiment and their disap-

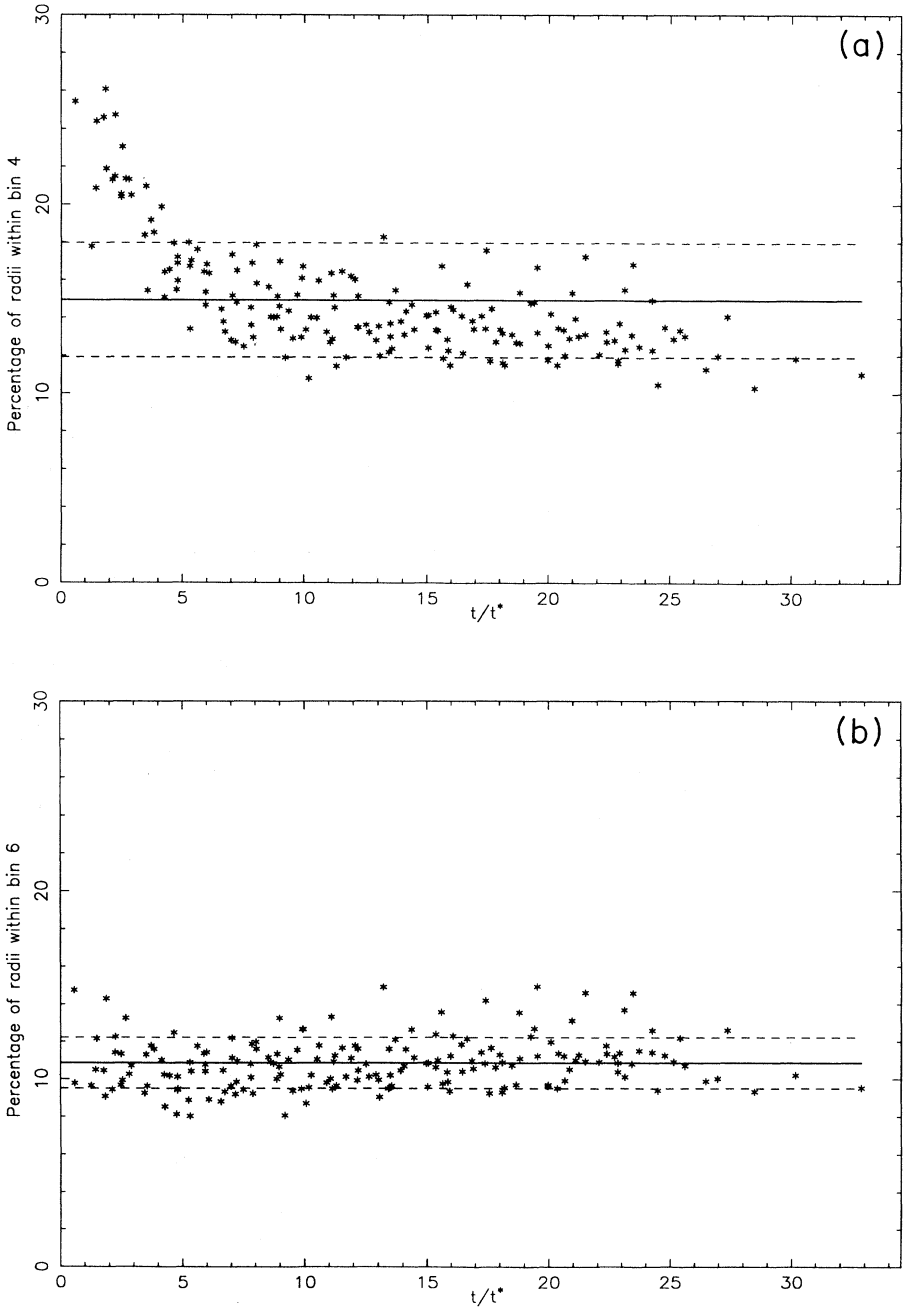

FIG. 8. (a) Time series of the percentage of the total "population" of radii that fall within the limits of bin 4. This image is characteristic of the variation observed in bins 3–5. These all show high initial populations relative to the other length scales. The average percentage (14.9%) is indicted by the solid line. The standard deviation (3.0%) is marked by the two dashed lines. (b) Time series of the percentage of the total "population" of radii that fall within the limits of bin 6. This image is characteristic of the variation observed in bins 2, 6, 7, and 8, which remain constant with time. The average percentage (10.9%) is indicated by the solid line. The standard deviation (1.4%) is marked by the two dashed lines. (c) Time series of the percentage of the total "population" of radii that fall within the limits of bin 9. This image is characteristic of the variation observed in bins 1 and 9, both of which increase with time. The average percentage (19.6%) is indicated by the solid line. The standard deviation (1.6%) is marked by the two dashed lines.

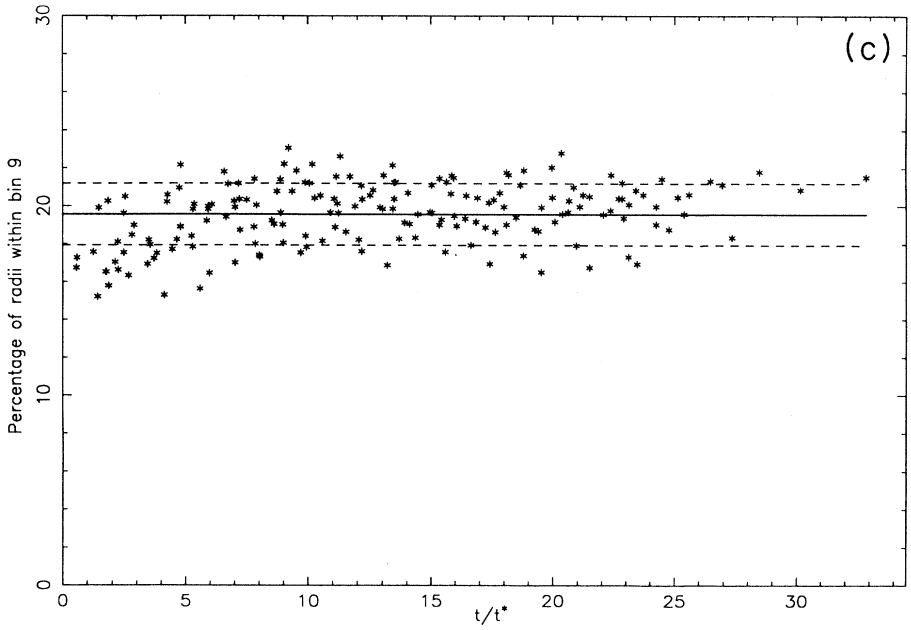

FIG. 8. (*Continued*).

pearance at later times is emphasized by the decreased prominence of the large bin between -0.5 and 0.5 and the disappearance of the dominant small bin peak at ± 0.5 [Fig. 10(c)]. The other dominant modes, seen in Figs. 10(b) and 10(c) occur at values slightly larger than ± 1 and ± 2. These modes are more pronounced in the histogram from the later time [Fig. 10(c)] due to the dissipation of the small scales and the values of the dominant modes in Figs. 10(b) and 10(c) contrast those of the slower flow [Fig. 10(a)], which were somewhat smaller. Thus a modal behavior appears that consists of scales partitioned like $\pm I_c'/2, \pm I_c'$, and $\pm 2I_c'$, where I_c' denotes the observed modes. It has also been observed that I_c' increases with respect to I_c as the flow rate is increased. This may be a manifestation of wetting effects that are not accounted for in Eq. (3) used to predict I_c. These wetting effects should become more pronounced at higher flow rates, leading to larger characteristic length scales [7].

DISCUSSION

This study has focused on characterizing the fingering patterns formed when air is injected into a silicon oil contained within a rectangular Hele-Shaw cell. A range of injection rates was used, but due to limitations imposed by the cell geometry and the occurrence of pinch-off events at higher flow rates which limited the maximum

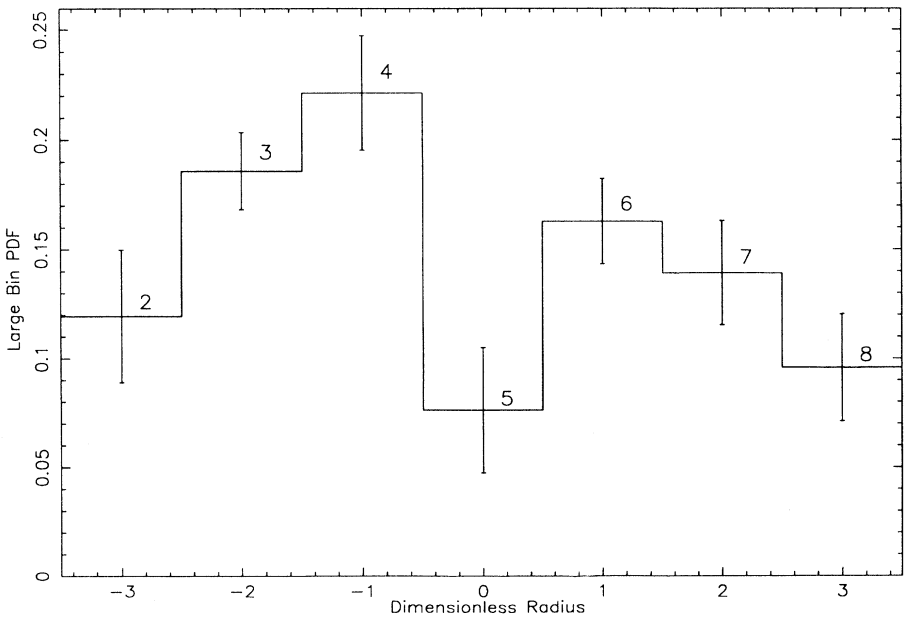

FIG. 9. Average histogram for data of entire experiment. Error bars are shown indicating the variability present in each bin. Each bin has been labeled according to the designation assigned to it in Table II.

flow rate, the range of length scales was limited to 1.5 orders of magnitude. The achievable range in injection rates was insufficient to generate an observable flow-rate dependency (as reported previously in [9]), in power-law variables, which were generated from regressing various flow characteristics (L_i, H_f, and R_g, Fig. 4) against the flow area for the time series generated for each run. The average values, over all the runs of the experiment, for the three power relations are essentially identical, indicating that the side walls of the cell were a dominant factor in determining the development of the flow patterns. This is most strongly indicated by the fact that the power relation based on L_i, which should be 2D in nature, is indistinguishable from the power-law variables for H_f and R_g, which are essentially 1D. This effect of the side walls is also witnessed in the superposition of the $\rho(y)$ curves [Fig. 3(b)] and the curvature plots [Figs. 7(b) and 7(c)] both of which show the regions of growth to be near the top of the flow pattern, farthest from the injection point, indicating that the side walls quickly become restrictive, forcing the majority of the growth to occur parallel to the boundaries.

The area and interfacial dimensions calculated for these patterns have ranges of 1.76–1.84 and 1.04–1.22, respectively. A time-independent interfacial dimension of 1.39 has been reported in a previous work [12] for a

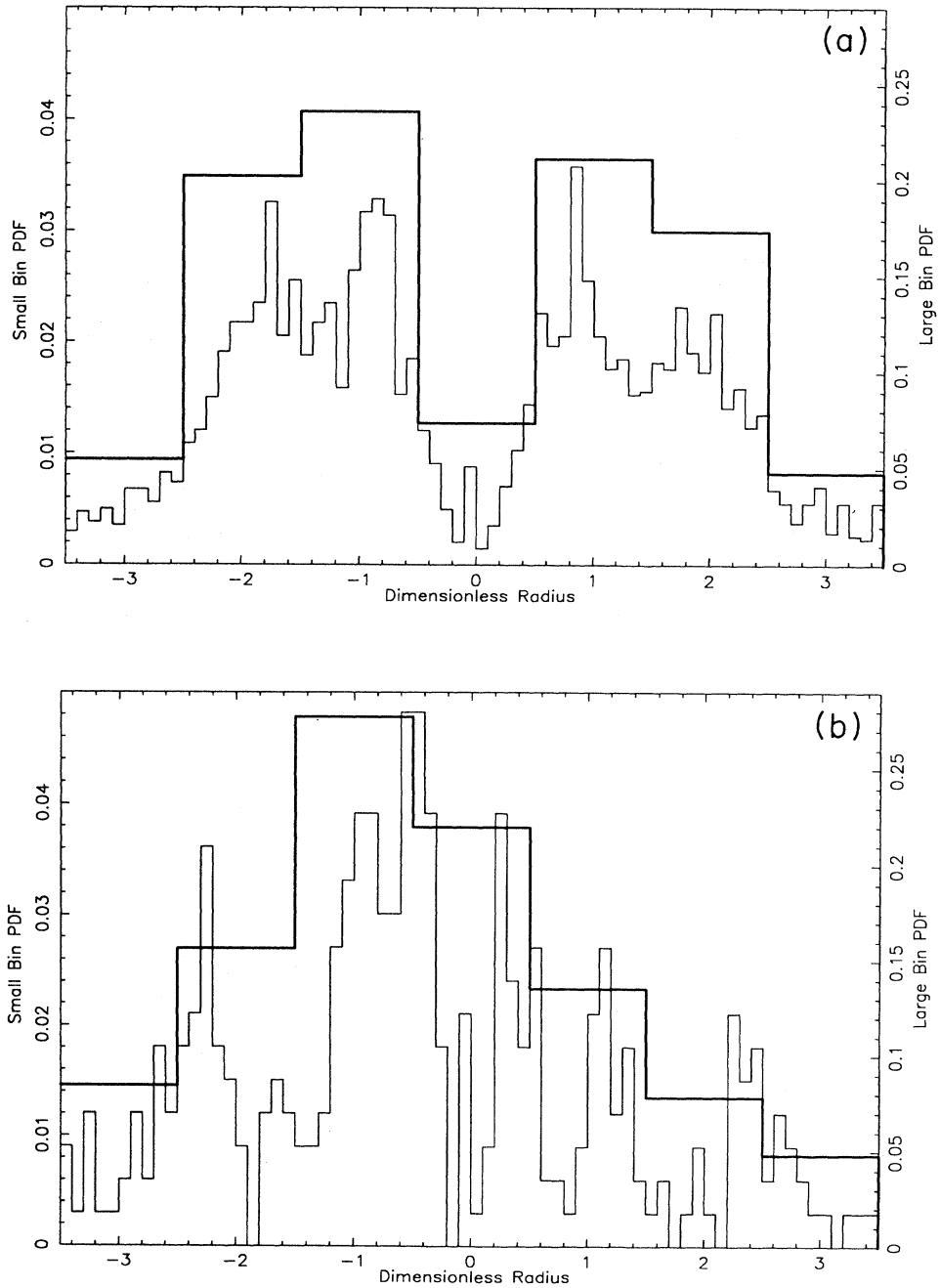

FIG. 10. (a) Histograms for frame 10 of a run at the slowest flow rate. The high-resolution histograms have bin sizes of $0.1I_c$. Note the peaks at values slightly less than $\pm I_c$ and $\pm 2I_c$. The coarse resolution histograms have bin sizes of $1.0I_c$, which are centered around 0.0, $\pm 1.0I_c$, $\pm 2.0I_c$, and $\pm 3.0I_c$. These are useful in investigating the bulk properties of the length scale distributions around the dominant instability modes. Note the peak that occurs around $\pm I_c$ and the tendency for the negative bins to be higher than their positive counterparts. (b) Histograms for frame 1 of series shown in Fig. 7(a). Note the dominant modes that have shifted to values slightly greater than $\pm I_c$ and $\pm 2I_c$, in contrast to the dominant modes reported from Fig. 9(a). In addition, note the appearance of prominent peaks around $\pm I_c/2$ and the dominance of the large bin centered on 0. These features illustrate the elevated small scale populations that are characteristic of all the initial images of each run of the experiment. (c) Histograms for frame 10 of series shown in Fig. 7(a), a later time of the same run from Fig. 9(b). Note the persistence of the dominant modes at values slightly greater than $\pm I_c$ and $\pm 2I_c$ and the significant reduction in the presence of scales around $\pm I_c/2$.

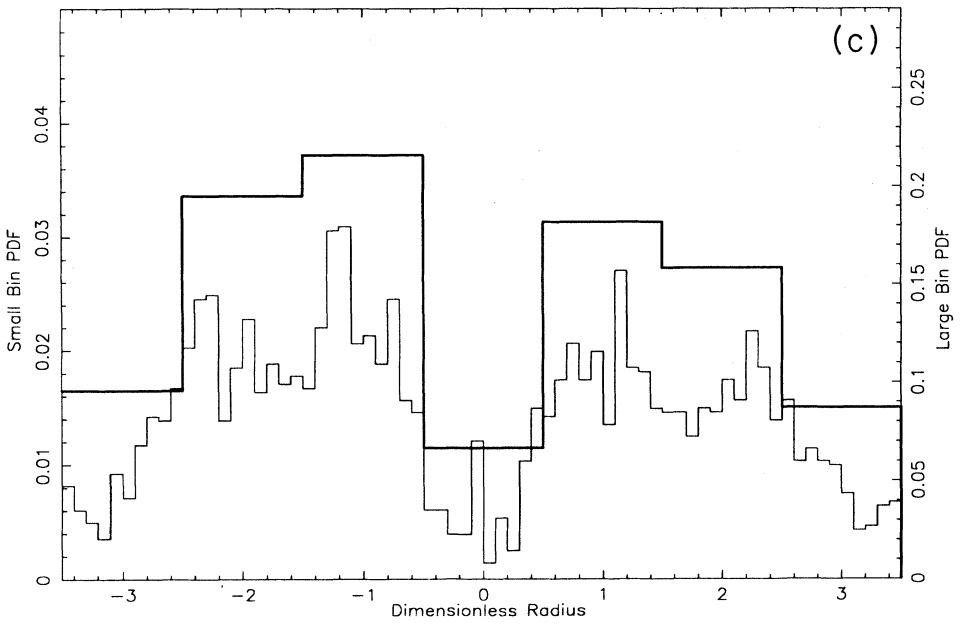

FIG. 10. (*Continued*).

case without surface tension. This supports the contention that fractal or stochastic behavior is diminished in the presence of a stabilizing mechanism, in this case surface tension. The range in interfacial dimension witnessed in this experiment is due to the limited range of length scales which exacerbates the inherent difficulty, when using the stick method, of obtaining the well-defined straight line necessary for defining a fractal dimension (Fig. 5). Despite claims in the literature, easily defined slopes are rarely realized with this technique [13]. The box-counting method is more appealing as a measure of fractal dimension, since the constant slope region is well defined. Nevertheless, though the values of the two dimensions have no relationship and despite the range of the interfacial dimension, the temporal variability of the two dimensions appears to coincide. The temporal variation emphasized by the fitted polynomial curve (Fig. 6) reveals the values of D_a to be increasing and values of D_i to be decreasing. The strong initial decrease in D_i from values of ~ 1.17 down to an asymptotic value of ~ 1.07 by $t/t^* = 10$ [Fig. 6(a)] indicates that the patterns are becoming "less fractal" as the flow evolves, since, as D_i tends toward 1.0, the interface tends toward a straight line. Similarly, since a value of 2.0 represents the Euclidean area dimension, the greater the deviation of D_a [Fig. 6(a)], the more fractal the object. Thus, since D_i and D_a vary inversely, they both indicate the flow patterns to be more fractal at early times before reaching patterns to be more fractal at early times before reaching asymptotic values of 1.08 for D_i and 1.79 for D_a at $t/t^* = 20$.

The results obtained from the histogram analysis indicate (1) a temporal behavior in populations of the largest and smallest scales, (2) an overall behavior consisting of more negative than positive scales, and (3) a modal behavior in the dominant length scales. The observed variations of percent population in the nine bins (Table II) reveal a tendency toward longer length scales as time progresses (Fig. 8). This reflects both the overall expansion of the pattern, which results in long smooth interfaces on the shielded sides of the pattern, and the smoothing of the previously generated small scales through the action of surface tension. The average histogram (Fig. 9) reveals the negative scales to be dominant, with the dominance progressing from negative bin to corresponding positive bin, except for bin 6, which is not greater than bin 3. In addition, the smaller scales are more populous than the larger scales. The modal behavior witnessed in the small bin histograms consists of peaks at $\pm I_c'$ and $\pm 2I_c'$, with scales at $\pm I_c'/2$ appearing at the early times of each run [Fig. 10(b)]. It also appears that as the flow rate increases, the observed value of the modes increases with respect to the value predicted using the linear stability derived relation [Eq. (3)]. A flow-rate-independent difference between the observed modes (I_c') and the predicted modes (I_c), would indicate that the estimated interfacial velocity used to calculate I_c was incorrect but that the linear theory itself, using the *ad hoc* boundary condition [Eq. (4)], was adequate. The fact that the difference between the observed and predicted modes is not constant with flow rate indicates that wetting effects are non-negligible, with a tendency toward length scales larger than the prediction of the linear theory. This agrees with previous results [6,7], which show decreasing maximum wave number (i.e., increasing threshold length scales) with increasing flow rate.

ACKNOWLEDGMENTS

J.W. would like to thank Dr. Geoff Spedding for his extremely helpful assistance in computer programming, and Dr. Fred Browand and Dr. Eckart Meiburg for their useful comments and insights. This work was supported by ONR Grant No. N00014-86-K-0679.

[1] R. L. Chouke, P. van Meurs, and C. van der Poel, Petrol. Trans. AIME **216**, 188 (1959).
[2] P. G. Saffman, and G. Taylor, Proc. R. Soc. London, Ser. A **245**, 312 (1958).
[3] G. M. Homsy, Ann. Rev. Fluid Mech. **19**, 271 (1987).
[4] C.-W. Park and G. M. Homsy, J. Fluid Mech., **139**, 291 (1984).
[5] D. A. Reinelt and P. G. Saffman, SIAM J. Sci. Stat. Comput. **6**, 542 (1985).
[6] L. Schwartz, Phys. Fluids **29**, 3086 (1986).
[7] T. Maxworthy, Phys. Rev. A **39**, 5863 (1989).
[8] T. Maxworthy, J. Fluid Mech. **177**, 207 (1987).
[9] S. N. Rauseo, P. D. Barnes, Jr., and J. V. Maher, Phys. Rev. A **35**, 1245 (1987).
[10] B. Mandelbrot, *The Fractal Geometry of Nature* (Freeman, New York, 1983).
[11] L. F. Richardson, Gen. Sys. Yearb. **6**, 139 (1961).
[12] J. Nittmann, G. Daccord, and H. E. Stanley, Nature **314**, 141 (1985).
[13] A. le Méhauté, *Fractal Geometries, Theory and Applications,* translated by J. Howlett (CRC, Boca Raton, 1990).

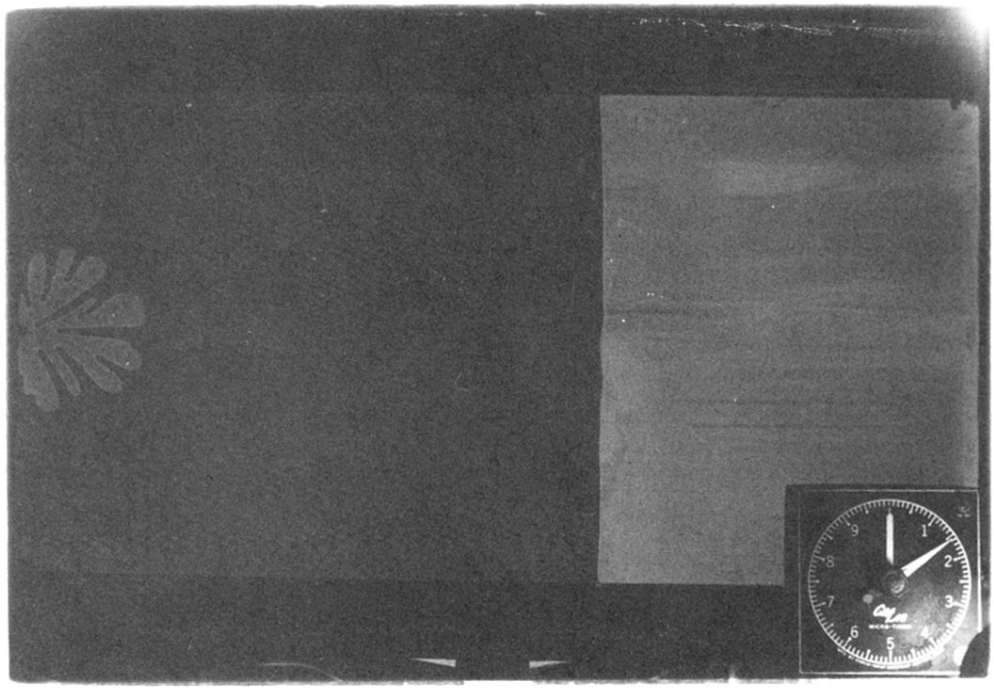

(a)

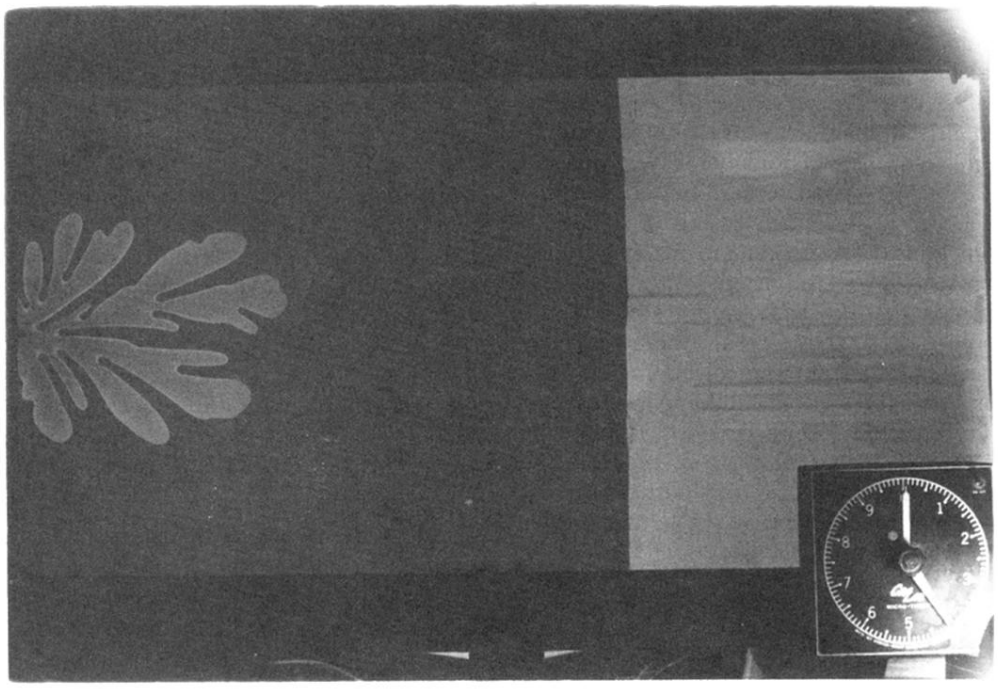

(b)

FIG. 2. (a) Frame 2 of a run from the highest flow rate. This picture illustrates the semicircular nature of the growth away from the injection port, before the presence of the side walls is felt. (b) Frame 5 of the same run. This picture shows the expansion to be essentially parallel to the side walls and the occurrence of a growth competition between two main fingers. (c) Frame 8 of the same run. This picture illustrates the pinching-off effect (the upper left portion of the pattern has become disconnected), which occurred for several of the runs at higher flow rates.

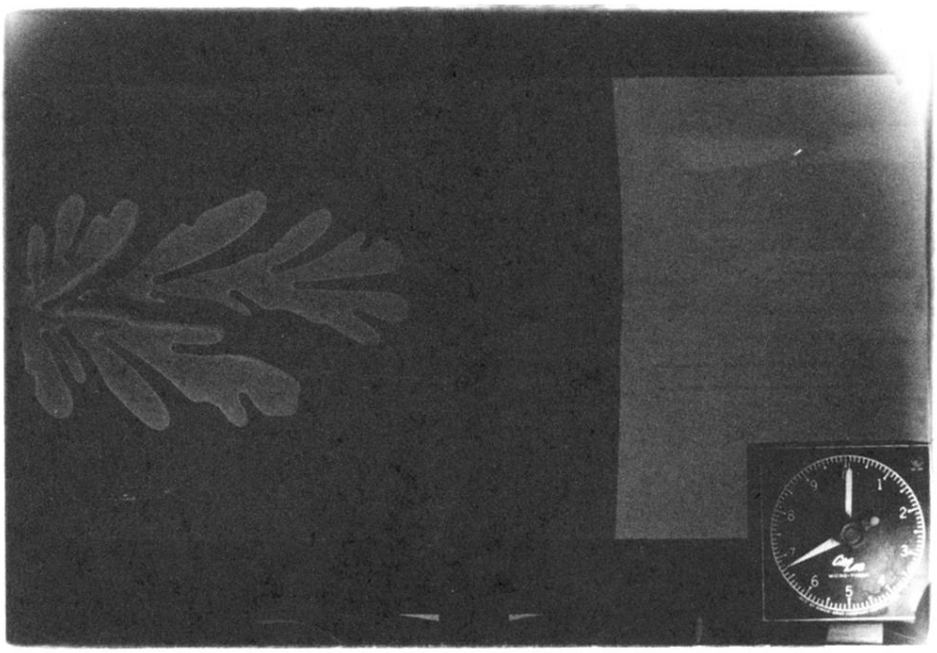

(c)

FIG. 2. (*Continued*).